

Journal of Materials Chemistry A

Materials for energy and sustainability

Accepted Manuscript

This article can be cited before page numbers have been issued, to do this please use: A. Susca, J. Liu, J. Cui, N. Mubarak, J. Wu, M. Ihsan-ul Haq, F. Ciucci and J. Kim, *J. Mater. Chem. A*, 2020, DOI: 10.1039/D0TA05298A.



This is an Accepted Manuscript, which has been through the Royal Society of Chemistry peer review process and has been accepted for publication.

Accepted Manuscripts are published online shortly after acceptance, before technical editing, formatting and proof reading. Using this free service, authors can make their results available to the community, in citable form, before we publish the edited article. We will replace this Accepted Manuscript with the edited and formatted Advance Article as soon as it is available.

You can find more information about Accepted Manuscripts in the [Information for Authors](#).

Please note that technical editing may introduce minor changes to the text and/or graphics, which may alter content. The journal's standard [Terms & Conditions](#) and the [Ethical guidelines](#) still apply. In no event shall the Royal Society of Chemistry be held responsible for any errors or omissions in this Accepted Manuscript or any consequences arising from the use of any information it contains.

ARTICLE

Affinity-Engineered Carbon Nanofibers as Scaffold for Na Metal Anodes

Received 00th January 20xx,
Accepted 00th January 20xx

DOI: 10.1039/x0xx00000x

Alessandro Susca,^a Jiapeng Liu,^a Jiang Cui,^a Nauman Mubarak,^a Junxiong Wu,^a Muhammad Ihsan-Ul-Haq,^a Francesco Ciucci^a and Jang-Kyo Kim^{a*}

Metal anodes possess the potential to disrupt the limits imposed by intercalation compounds and achieve a higher storage density for next-generation rechargeable batteries. This study is dedicated to engineering a scalable scaffold made of carbon nanofibers (CNFs) modified with embedded ZnO nanoparticles as facile nucleation sites for enhanced Na plating performance. The pristine CNF network provides a highly-conductive, mechanically-stable plating platform while the porous morphology effectively lowers the local current density and the volume fluctuations, delivering 1500 cycles at 1 mA cm⁻². In search of appropriate sodiophilic surface for stable Na plating, the affinities between Na and different substrate materials are analyzed by measuring overpotentials, Coulombic efficiencies, and through density functional theory calculations. The ZnO@CNF composite created by in-situ incorporation of ZnO nanoparticles offers uniform nucleation and deposition of Na through conversion and alloying reactions, leading to ameliorated cyclic stability at a high current density of 3 mA cm⁻². The Na plating thickness is predicted based on simple electrochemical principle and geometric considerations, corroborating experimental measurements. The affinity-engineered ZnO@CNF anodes deliver more than 1000 hr of stable plating/stripping cycles in a symmetric battery configuration by effectively inhibiting the growth of dendrites and Na agglomerates.

Introduction

The issues arising from repeated plating and stripping of alkali metals, especially Li and Na, have made their application in energy storage highly challenging. Metallic Li is widely used in primary batteries because of its high specific energy,^[1, 2] and Na has been successfully applied in high-temperature Na/S devices for stationary applications.^[3] However, the use of alkali metals in room-temperature rechargeable batteries has been limited to an intercalation or alloying-based chemistry since the release of the first Li-ion batteries almost three decades ago.^[4, 5] While such a chemistry ensures a high degree of stability by avoiding direct contact between the reactive alkali metal and the electrolyte, the practical specific capacities are much reduced from their theoretical values of 3,860 mAh g⁻¹ for Li and 1165 mAh g⁻¹ for Na.^[6, 7] In particular, Na-based batteries are considered more viable for long-term mass production than their Li counterparts due to several techno-economic reasons.^[8] Abandoning any host material and using Na in its elemental state do not come without challenges. Similarly to metallic Li,^[9-11] the growth of dendrites during the electroplating of Na is known to be a key challenging issue.^[12-14] Although the range of parameters influencing dendritic growth has yet to be fully

understood due to the experimental difficulties of characterizing such a phenomenon, the underlying mechanism can be summarized in light of recent studies,^[15-19] as follows. Metallic Na reacts with the liquid electrolyte creating a solid electrolyte interphase (SEI), whose composition and stability are highly dependent on both the solvent, the ionic salt and its concentration in the electrolyte.^[15-16] Electrochemical plating causes the depositing Na to nucleate on a limited number of rough sites on the current collector, where the electric field is higher than the surrounding flat area. The large volume fluctuation arising from the newly deposited Na leads to the formation of narrow cracks in the SEI layer, through which Na grows uncontrollably into dendrite-shaped protuberances. Possible outcomes after prolonged growth of dendrites are then (i) perforation of the separator and consequent short circuit during plating, and (ii) detachment of the dendrites and formation of "dead Na", which is then entirely isolated from the circuit.^[17] It can be concluded that an SEI layer with good chemical and mechanical stability can contain the growth of such an undesired dendrite structure.^[18] The current density heavily influences the process, with a low current density allowing Na to nucleate densely on the surface.^[19] Moreover, a low current density can decrease the probability of dendrites growth by avoiding large polarization and fast growth at the reaction front.^[8]

Research on Li metal anodes pioneered the field of metal anodes, leading to significant progress in suppressing the growth of dendrites and achieving uniform plating/stripping.^[6, 20, 21] Among several successful strategies, the current study is

^a Department of Mechanical and Aerospace Engineering, The Hong Kong University of Science and Technology, Clearwater Bay, Kowloon, Hong Kong.

* Corresponding author email: mejkkin@ust.hk

Electronic Supplementary Information (ESI) available: [details of any supplementary information available should be included here]. See DOI: 10.1039/x0xx00000x

mainly concerned with the following approaches. (i) The first one involves developing a conductive and mechanically stable matrix possessing a large surface area. Such a structure is able not only to drastically reduce the local current density - an important parameter for dendritic growth - but also to contain and accommodate the volume expansion upon repeated cycles. (ii) The second approach is to enhance the affinity between deposited alkali metal and current collector, resulting in a reduced nucleation energy to the advantage of dense nucleation against uncontrolled growth. These two strategies were also combined together to develop a 3D conductive scaffold with high affinity nucleation sites, achieving outstanding results for Li metal batteries.^[22-27] As for the Na counterpart, the benefits of high-affinity nucleation substrates have been proven in many studies, using a nanocarbon layer on an Al current collector,^[28] a gold film sputtered on a Cu collector,^[29] several different alloying metals^[30] and even a layer of silk-derived pyroproteins.^[31] 3D conductive networks such as carbon felt^[32] and carbon microspheres,^[33] porous copper^[34] and aluminum,^[35] were also proven to be effective. The two strategies have been simultaneously applied with carbon nanotube electrodes containing N- and S- functional groups,^[36] catalytic carbon nanotemplates,^[37] doped and porous carbon fibers^[38-39] where the substrate surface condition ameliorated the affinity to Na.

In summary, a low growth rate is essential to achieving stable Na plating/stripping cycles. An electrode possessing a large specific surface area (SSA) lowers the growth rate by increasing the active contact area for plating. Dense and favorable Na nucleation reduces the growth rate by increasing the number of growing nuclei instead. Here we present such a synergistic strategy to minimize the local current density and offer a large and favorable deposition surface through the use of a network of inexpensive carbon nanofibers (CNFs) whose morphology was engineered by incorporating myriads of sodiophilic zinc oxide nanoparticles (ZnO@CNF). The rationale behind the

choice of strategy is schematically illustrated in Figure 1. ZnO@CNFs act not only as a current collector having high affinity and a large SSA, but also as a 3D scaffold to accommodate the plated Na. We prove that a pCNF network even without any additional materials attached had a beneficial effect due to its large SSA and high porosity while ZnO possessed a higher affinity to Na than other commonly used materials like Cu and Al. We subsequently present the superior performance of ZnO@CNF as an affinity-engineered conductive scaffold.

Experimental

Fabrication of CNF films

CNFs were produced via electrospinning of a polymeric precursor, 5 wt% solution of polyacrylonitrile (PAN) in DMF. The precursor for ZnO@CNFs was prepared by adding 7.5 %wt of ZnAc₂ into the neat PAN solution. The zinc salt was dehydrated overnight in a vacuum oven at 135°C before adding into the solution. The precursor solutions were electrospun at a voltage of 18kV and a pump rate of 1 mL hr⁻¹ on a rotating collector drum. The freshly spun fibers were stabilized in an oven at 230°C for 3.5 hr in air, and carbonized in a tube furnace at different temperatures ranging 650 to 800 °C for 1 hr in a nitrogen atmosphere, with a temperature ramp of 2°C min⁻¹. The resulting CNF film was then cut into disk shapes of 14mm in diameter before being used as an electrode.

Substrates for Affinity Studies

Cu, Al, Mg and Zn were introduced as freestanding foils; Ag, Al₂O₃ and SiO₂ were thermally evaporated on a Cu foil; Pt, Ag and carbon were sputtered on a Cu foil; Sn was deposited on a Cu foil as a surface film from the high temperature decomposition of tin (II) acetate; ZnO was produced by oxidizing a zinc foil at 300°C for 10 hr.

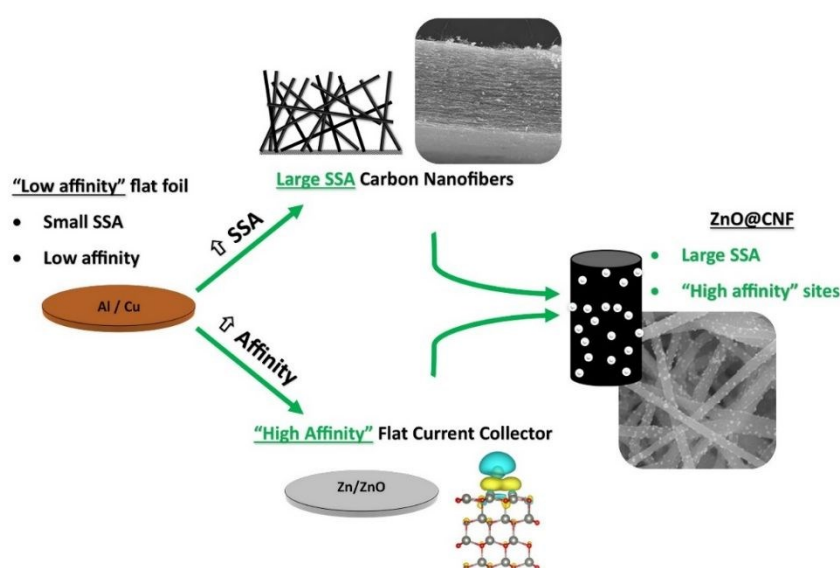


Figure 1: Schematic of synergistic rationale behind the ZnO@CNF electrode design.

Materials Characterization

The synthesized materials were examined under SEM (JSM-6700F, JEOL) and TEM (JEM 2010, JEOL). No conductive coating was applied to any of these materials before electron microscopy. The powder XRD analysis (PW1830, Philips) was carried out on flat current collectors, pCNFs and ZnO@CNFs at 2θ ranging between 10 and 80° . The thermogravimetric analysis (TGA, Q5000, TA Instruments) was performed in a nitrogen atmosphere from room temperature to 800°C , with a heating ramp of $10^\circ\text{C}/\text{min}$ up to 600°C , and of $2^\circ\text{C}/\text{min}$ from 600°C to 800°C . The sheet resistance of CNF films was measured on a Hall effect measurement system (Ecopia HMS-5500). The surface functionality was investigated with XPS (Axis Ultra DLD, Kratos Analytical). The nitrogen adsorption/desorption isotherms were obtained on an automated adsorption apparatus (Micromeritics, ASAP 2020) to measure the BET surface area and porosity.

Electrochemical Characterization

All electrochemical tests were conducted using CR2032 coin cells assembled in an Ar-filled glovebox. The different cell setups are shown in Figure S1. Half cells were prepared using the CNF film as a freestanding working electrode without adding a current collector, and a Na foil as reference and counter electrodes. All electrodes for CE tests were cut into discs of 14mm in diameter for working electrodes and 16mm for counter electrodes. Overpotentials were measured based on the same half-cell configuration, but using the said substrates as working electrodes. For symmetric cells, ZnO@CNF was stacked on top of Na foil and served as both working and counter electrodes. The control cells were prepared using a pure Na foil as both working and counter electrodes. All electrodes for symmetric cells were cut into discs of 14 mm in diameter. The electrolyte was prepared from 1M NaCF₃SO₃ in diglyme for all experiments, except for the carbonate-electrolyte cells where the electrolyte was prepared using 1M NaClO₄ in EC:PC (1:1). 80 μL of electrolyte were typically used. A single polymeric separator (Celgard 2400) was used for all experiments, except for the carbonate-electrolyte cells where a glass fiber separator (Whatman GF/D) was used after cutting into discs of 18mm in diameter. Electrochemical impedance spectroscopy (EIS) measurements were conducted of symmetric cells with frequencies ranging from 10.0 mHz to 100 kHz.

Results and Discussion

Na Plating on pCNFs with a Large Surface Area

A network-like current collector possessing a good electrical conductivity, a large SSA and stable mechanical properties is a likely candidate to suppress dendritic growth and enable uniform Na plating and stripping during repeated cycles. Carbon nanomaterials are an obvious choice to satisfy such requirements, thanks to their highly-tunable morphology and intrinsic electrical and mechanical properties.^[40, 41] Since the choice of Na over Li is dictated mainly by economic

consideration, it follows then that the choice of current conductor should also consider price and availability as key factors. Electrospun CNFs are relatively inexpensive, easy to process and viable to scaling-up to an industrial scale.^[42, 43] Moreover, the produced CNF current collectors are freestanding and do not require additional binder or metallic foil for use as electrodes.

The CNF network was realized by electrospinning of a polyacrylonitrile (PAN) precursor dissolved in dimethylformamide (DMF). The material and process parameters of electrospinning were carefully controlled to obtain a flexible film of $\sim 100\ \mu\text{m}$ in thickness after carbonization. While the performance of CNFs carbonized at different temperatures was very similar at a low current density of $1\ \text{mA cm}^{-2}$, the difference in cyclability became considerable with increasing current density (Figure S2), probably due to the different electrical conductivity of the different samples. The electrical conductivity was measured to be 4.0×10^{-4} , 3.6×10^{-2} and $1.6\ \text{S m}^{-1}$ for the samples carbonized at 650, 725 and 800°C , respectively. After extensive trial and error, 800°C was chosen as the carbonization temperature in this study. The CNFs after carbonization were randomly dispersed and had 100-150 nm in diameter, as shown in Figure 2a and S3. The X-ray diffraction (XRD) pattern confirms that the carbon in the fibers was mostly amorphous (Figure S3), as expected from the low carbonization temperature of 800°C .^[44] The Brunauer–Emmett–Teller (BET) surface area of the CNF film measured using a nitrogen adsorption/desorption test was $16.9\ \text{m}^2\ \text{g}^{-1}$.

The electrochemical performance of neat CNF anodes was evaluated in a half-cell configuration versus pure Na, see the cell schematics presented in Figure S1. A single layer of polymer separator, Celgard 2400, was used to maintain the experiment close to practically scalable conditions. It is assumed that the use of multiple layers or of thick separators would unrealistically delay the battery failure, when that happens by dendrites-induced short circuit. The *ex-situ* SEM image of CNFs taken after Na plating at $1\ \text{mA cm}^{-2}$ presented a moderate degree of Na agglomeration especially at the fiber junctions, with small agglomerates dispersed along the fiber length, as shown in Figure 2b. This observation indicates that the CNFs film functioned as a current collector with a large SSA effectively reducing the local current density during the deposition of Na. The Coulombic efficiency (CE) in a half-cell configuration is a measure of available plated Na, and a stable CE signifies uniform and reversible plating and stripping. The CE of the CNF network as a freestanding anode is compared with the one using a flat carbon-coated Cu current collector at a current density of $1\ \text{mA cm}^{-2}$, as shown in Figure 2c. The CNF current collector was cycled for almost 1600 full cycles with a very stable average CE of over 99.6%, whereas the latter metal current collector exhibited highly fluctuating CEs even from the first cycle and an overall life of less than 400 cycles before experiencing a short circuit. The capacity-voltage curves of the first 10 cycles are shown in Figures 2d and 2e for the flat carbon current collector and the CNF respectively, highlighting several chaotic voltage peaks during stripping of the flat metal current collector and a contrasting stable voltage profile of the 3D fiber network. In the

case of flat carbon, only the plating curve (negative voltage) and the stripping curve with chaotic peaks were detected. Essentially the same behavior as the flat carbon is shown in Figure S4 for a flat Cu current collector without a carbon coating. For the CNF electrode, brief Na insertion and extraction portions appear before plating and after stripping, respectively. To understand how the increasing SSA could slow the Na growth during plating, the thickness of deposited Na on the two different current collectors was estimated. The surface area of a flat disk-shaped current collector was 1.54 cm^2 . Based on the typical areal loading of the CNF electrode and its Brunauer-Emmett-Teller (BET) surface area, the total surface area of one CNF current collector was estimated to be $\sim 254 \text{ cm}^2$, which is 165 times larger than the flat counterpart. For example, assuming an ideal case in which plating happens uniformly on all the available surface, a $10 \text{ }\mu\text{m}$ thick layer plated on the flat current collector would be redistributed through the whole CNF network to obtain only about 60 nm thick plating. The fast and large volumetric increase of Na on a flat current collector is thus likely to result in the formation of dendrites with a rough morphology. These can perforate the separator during plating or lose contact with the current collector during stripping, as suggested by the chaotic voltage profile during charging (Figures 2d), leading respectively to a short circuit or to a permanent loss of capacity.

The current density is among the main factors influencing the stability of an alkali-metal battery in a long term cyclic experiment, showing a sharp decrease in lifetime with increasing current density for both Li ^[45, 46] and Na storage.^[47, 48] To understand the performance of our materials at their limiting current, the half-cell cyclic tests were performed at a higher current density of 3 mA cm^{-2} with an increased loading of 3 mAh cm^{-2} . The long-term cyclic behavior at this current was severely destabilized as seen from the CE results in Figure S1.

The best CNF cell survived less than stable 300 cycles, after which an irreversible capacity loss prevailed. It appears that even the large SSA of the CNF electrode was unable to lower the local plating rate at such a high current density. It follows then that the nucleation of Na had to be ameliorated by enhancing the Na-affinity of the fibers.

Na Plating on Substrates with Different Affinities

Nucleation, the first step during deposition, requires a relatively high energy for the creation of an interface between Na and the substrate. When depositing at a constant current density, a temporary overpotential is needed to provide the first nucleation energy, whose magnitude is dictated by how difficult the interfacial relaxation is. The mechanism behind the plating behavior is summarized in Figure 3a. This observation means that the deposition overpotential can represent the affinity between the two materials. Such a strategy has already been widely implemented for Li ^[26, 49-51] and Na ,^[27-29, 35] showing that a reduced overpotential led to a denser nucleation during deposition. In an effort to identify favorable species, the overpotentials of a wide range of materials, including Cu, Al, Al_2O_3 , SiO_2 , Au, Ag, Pt, Mg, Sn, Zn and ZnO, were evaluated at a low current of $30 \mu\text{A}$. The initial overpotential was found only if the substrate was previously completely stripped of any residual Na, while partial stripping led to a zero-overpotential plating (Figure S5). This confirmed that the overpotential was indeed directly related to the creation of a new interface. Moreover, for some selected materials, the overpotentials method was corroborated by the evaluation of CE values and the *ab-initio* calculation of adsorption energies.

The overpotential values for the different substrates are summarized in Table 1. The voltage behaviors over time showing the overpotential differences are given in Figure 3b for several different materials. Similar data for all other substrate

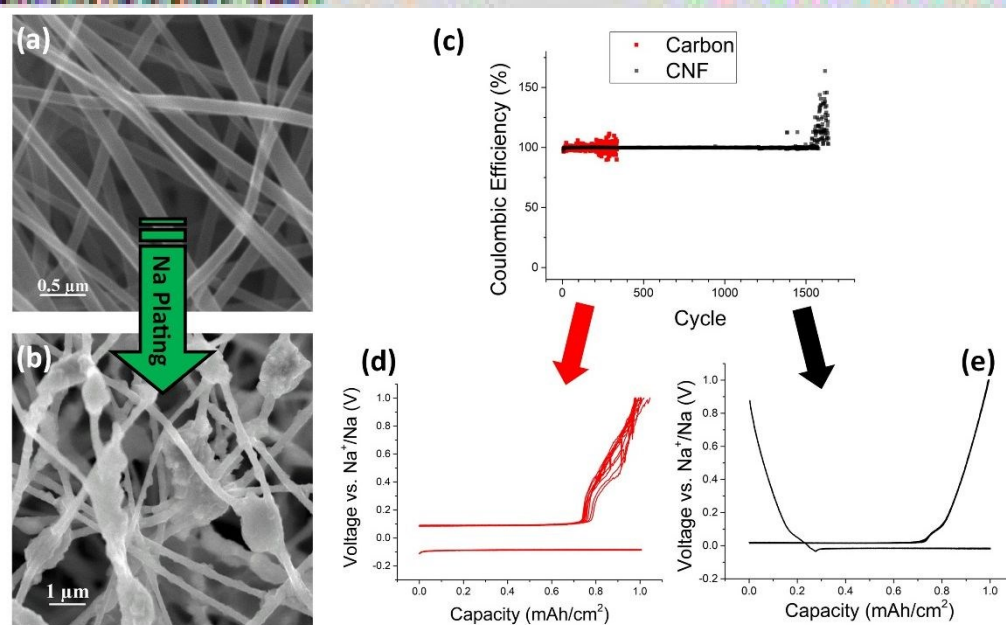


Figure 2: SEM images of CNF network (a) before and (b) after Na deposition with a loading of 0.15 mAh cm^{-2} . (c) Coulombic efficiencies of flat carbon and CNF network electrodes measured using a half cell configuration against Na at a loading of 1 mAh cm^{-2} and a current density of 1 mA cm^{-2} . Voltage variations in the first 10 plating/stripping cycles of Na on (d) a flat carbon current collector and (e) a CNF network, measured at a current density of 1 mA cm^{-2} .

materials are shown in Figure S6. It is important to notice that none of these materials had a zero-overpotential interaction with Na, as opposed to Li which is known to have high affinity with several metal substrates, such as Au.^[26] Among them, Zn and Sn exhibited the lowest overpotentials of 4 and 3 mV, respectively, for Na deposition, followed by ZnO and Au both with 7 mV. In contrast, a very high overpotential of 20 mV was necessary to deposit Na on Cu and Al. Previously, Au Sn and Zn were found to have high affinity for Na nucleation.^[28, 29, 52]

Table 1: Overpotentials of different metals for deposition of Na, measured at a constant current of 30 μ A in a half-cell configuration. Overpotentials were approximated to the closest unit according to the experimental accuracy.

Materials	Overpotential [mV]
Cu	20
Al	20
SiO ₂	11
Carbon	10
Al ₂ O ₃	10
Ag	10
Mg	10
Pt	10
Au	7
ZnO	7
Sn	4
Zn	3

The Coulombic efficiencies of Zn and ZnO current collectors upon repeated Na plating/stripping cycles are shown in Figure 3c in comparison with those of Cu and Al. It is important to note that the flat metal current collectors with a small surface area were subjected to a relatively high local current density and their CE's were not as stable as for the 3D CNF counterparts. In fact, the *ex-situ* SEM image in Figure S7 shows that Na deposition on a Zn plate was predominantly of dendritic nature, similarly to that on Cu. However, while such a structure on a Cu plate tended to vertically accumulate to form mountain-like deposits (see later discussion on Figure 5a and 5b), the dendrites deposited on a flat Zn plate were dispersed throughout the whole electrode surface. Hence, the chance to lose contact with the collector and generate "dead Na" would be low. Consequently, there were few irreversible capacity losses for over 1000 cycles for Zn and for over 800 cycles for ZnO, whereas the capacity loss became evident within the first few cycles for Al and in less than 200 cycles for Cu.

Density functional theory (DFT) was explored to quantify the adsorption energies of Na on the said substrates. Vienna *ab-initio* simulation package (VASP) was used to simulate the interaction between Na and carbon, Zn, ZnO, and Sn. The calculation results indicate that Na adsorbs more favorably on the (0001) surface of ZnO or Zn than on the pure carbon surface. The adsorption energies of Na were -1.20, -0.98 and -0.44 eV on ZnO (0001), Zn (0001) and carbon, respectively, confirming better affinity of Na with the former two substrates than the latter. Figure 3e plots the electron density differences obtained

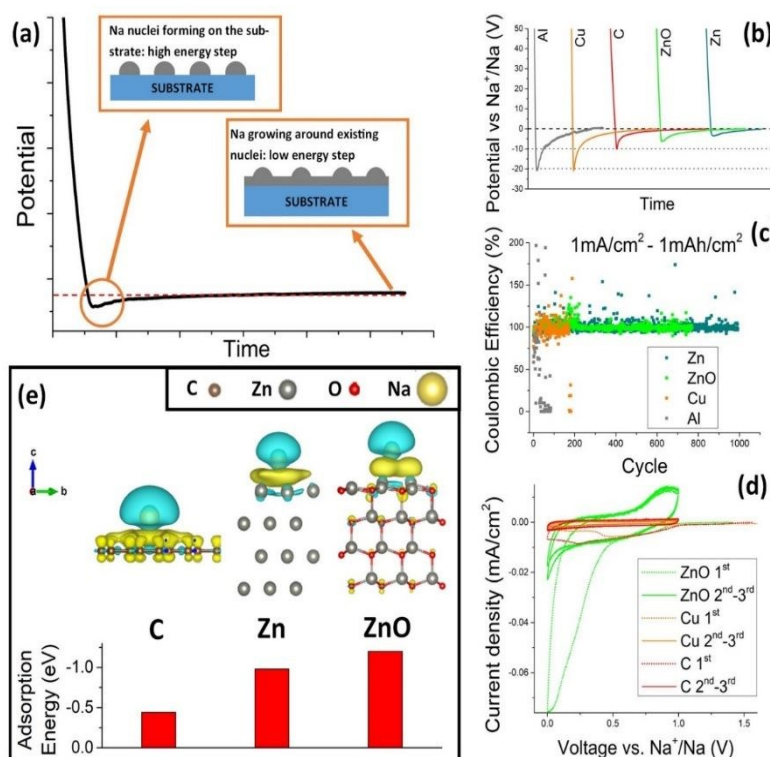
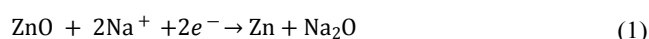


Figure 3: (a) Typical voltage profile of Na deposition highlighting two steps with an overpotential in the first nucleation step and steady state low voltage in the second growth step; (b) Voltage changes vs Na⁺/Na over time for Na deposition on different substrates at a constant current of 30 μ A; (c) Coulombic efficiencies of different substrates measured during repeated charge/discharge cycles at 1 mA cm⁻² in a half-cell configuration; (d) Cyclic voltammetry of half cells with ZnO and Cu vs. Na⁺/Na between 0 and 1 V at a scan rate of 0.1 mV s⁻¹, where the dashed lines correspond to the first cycle and the solid lines to the second and third cycles. (e) Electron density differences of Na adsorption on carbon, Zn and ZnO according to the DFT calculations and their adsorption energy.

from the calculations. According to the electrochemical measurements, Sn exhibited the lowest deposition overpotential which corroborates with the high adsorption energy of -1.25 eV for the Sn (001) surface, the highest value among all substrates studied here. More information on the DFT calculations can be found in Note S1, along with Figures S8 and S9.

Cyclic voltammetry (CV) was employed to investigate the interaction between Na and the current collectors at different voltages, as shown in Figure 3d. While carbon presented a slightly larger hysteresis than Cu, ZnO was the only material showing major reaction peaks. A broad anodic peak was noted at 1V, descending almost close to 0V, and a cathodic peak appeared between 0.75 and 1.0 V. This finding is consistent with previous reports on ZnO for Na-ion batteries.^[53-55] Previous *in-situ* studies proposed a two-step reactions:



where $x = 13$ for a full alloying reaction.^[56, 57] The cited studies identified all phases given in Equations (1) and (2) using *in-situ* transmission electron microscopy (TEM) and selected area (electron) diffraction (SAED) analysis of ZnO nanowires during their sodiation. The NaZn_{13} phase could not be detected using the *ex-situ* XRD analysis in this study, because its thickness failed to generate a strong signal. However, the reaction (1) of ZnO with Na was detected by the *ex-situ* XRD analysis, as shown in Figure S10. The same ZnO substrate was characterized before and after discharge to 5mV, and the results signified a large increase in metallic Zn signal after the electrochemical process, a reflection of ZnO converting to metallic Zn. Zn could then alloy with Na upon plating, facilitating the nucleation on the substrate.^[26, 29] Prominent peaks of Na_2O , a product of the proposed reaction between ZnO and Na, were also noted from the XRD pattern. Moreover, the current density in the CV experiment sharply increased when the ZnO cell approached 0V: at 1 mV, the current density for ZnO was 12 and 7.5 times higher than the ones for Cu and carbon, respectively. Such a sharp increase was associated with the lower deposition overpotential of Na on ZnO, enabling it to be plated at a higher voltage than on less sodiophilic surfaces.

ZnO@CNF with Enhanced Na Affinity

One of the main advantages of electrospun nanofibers is their tunable properties, where incorporating different types of materials at the precursor level can *in-situ* insert desired effects.^[58-61] Dehydrated zinc acetate (ZnAc_2) was added to the PAN/DMF precursor solution to obtain a final product with high-affinity ZnO nanoparticles embedded in the fibers. Although the metallic Sn and Zn appeared to be the best choices in terms of overpotential, incorporating them in the nanoscale fibers was found to be highly challenging. Both elemental Sn and Zn are present in the liquid state at the temperature necessary for carbonizing the electrospun nanofibers,^[62] hence these metals tended to severely agglomerate. Thus, we have chosen ZnO nanoparticles to incorporate in CNFs in this study. The freshly

electrospun fibers were stabilized at 220 °C in air before final carbonization: after stabilization ZnAc_2 was found decomposed into ZnO (XRD pattern in Figure S11). The rationale behind the optimization of the processing parameters is reported in Note S2, along with Figures S12, S13 and S14: a ratio of ZnAc_2 to PAN of 3:2 was chosen, along with a carbonization temperature of 725 °C.

The ZnO@CNF maintained a similar average diameter to the pCNF (~150 nm), and contained ZnO nanoparticles of 30-40 nm in diameter uniformly dispersed within and on the surface of fibers, as shown in Figure 4a and S15. The SAED patterns and the high-resolution TEM (HRTEM) images confirmed the hexagonal phase of ZnO (Figure 4b). The electrical conductivity was $5 \times 10^{-2} \text{ S m}^{-1}$ while the BET surface area was measured to be $7.1 \text{ m}^2 \text{ g}^{-1}$, which is much smaller than the pCNFs due to the higher density of fibers containing ZnO particles. The overall ZnO@CNF film thickness was ~100 μm. High resolution X-ray photoelectron spectroscopy (XPS, Figure S16) was used to probe the surface chemistry of CNFs with and without ZnO. Zn 2p and Zn LMM peaks at binding energies of 1021.9 and 498.1 eV were evidence of the presence of ZnO in ZnO@CNF. The deconvoluted carbon 1s peak was very similar for both pCNF and ZnO@CNF, suggesting that the addition of ZnO did not cause significant changes in the carbon surface functionalization. In order to investigate the internal distribution of ZnO nanoparticles, the fiber film was decomposed in air at 700 °C to obtain residual ZnO. The residual film was characterized by an interconnected network of ZnO nanoparticles (Figure S17) whose diameters were slightly larger than those within the fiber, indicating the ZnO particles were uniformly dispersed within the fiber network and coalesced during the decomposition of carbon matrix. The morphology of the ZnO@CNF electrode was examined by *ex-situ* SEM after 200 plating/stripping cycles, exhibiting structurally durable electrode with intact fiber networks and attached ZnO particles (Figure S18). The performance of the material was then evaluated through three stages: Na nucleation and its implication, Na plating behavior, and the long-term stability after Na infusion.

Electrochemical Performance of ZnO@CNF Electrodes. Figure 4c shows the typical plating/stripping voltage profiles of the pCNF and ZnO@CNF electrodes and explains how the increased affinity ameliorated the Na deposition by increasing the nucleation density over the fiber network. The effectively reduced overpotential of the ZnO@CNF electrode meant electrochemically active ZnO nanoparticles with high sodiophilicity. The activity of the ZnO nanoparticles could also be signaled by the increase in discharge capacity in the range between 1 and 0 V, respectively from 190 to 300 μAh cm⁻² for pCNF and ZnO@CNF. Figures 4d and 4e present *ex-situ* SEM images of pCNF and ZnO@CNF respectively, after a first discharge to 0 V. Under these discharge conditions, the nucleation of Na already started occurring, as suggested by the negative growth of current in the CV curves (Figure 4g). Only an initial part of nuclei appeared at a voltage above 0 V, leaving most of fibers still “naked”, thus providing explicit visualization of the difference in nucleation density. The majority of pCNFs

were uncovered with few nuclei and random agglomerates appearing in the network, see the larger overview of the same sample in Figure S19. Most nucleation occurred at the fiber junctions, a similar observation to previous reports for Li.^[21] In contrast, the ZnO@CNF electrode exhibited a large number of nuclei under the same conditions, which covered almost the entire CNF network.

The beneficial effect of increased nucleation density could be proven by the stable Coulombic efficiency of the ZnO@CNF electrode during long-term cycles at 3 mA cm⁻² and 3 mAh cm⁻² (Figure 4f): ZnO@CNF survived up to 700 stable cycles. Although the CE did not reach 100% as reliably as when testing at a lower current, the tested cells showed a significant delay in irreversible capacity loss compared to the pCNF electrode. The performance of the electrode is compared to the current state-of-the-art counterparts in Table S1. The ZnO@CNF performance at a high current of 3 mA cm⁻² and a high capacity of 3 mAh cm⁻² with 700 stable cycles, which corresponds roughly to 1600 hr of testing, is among the best and hardly matched by any reported materials. Similarly to the results obtained for a flat ZnO current collector, a conversion reaction was detected via XRD and CV analysis. The XRD pattern of the ZnO@CNF discharged to 5 mV lost the characteristic ZnO reflections and some of the Zn and Na₂O peaks are now visible, as shown in Figure S11. Figure 4g presents the CV curves for half cells with pCNF and ZnO@CNF electrodes during the first three cycles. The ZnO@CNF electrodes exhibited a broad anodic peak at ~1V and a cathodic

peak at above 0.75V, corresponding to the conversion reactions previously described. These peaks were absent for the pCNF electrode. The current density at a voltage of 1 mV was more than twice as high for ZnO@CNF than for pCNF, signifying much favored plating in the former electrode. The CV curves obtained using symmetric cells at voltages ranging between -0.1 and 0.1 V are shown in Figure 4h. The voltage-current slopes were over twice as large for ZnO@CNF than for pCNF, i.e. 120 versus 55 mA V⁻¹ for linear fits after the first cycle, confirming a much lower resistance to plate for the ZnO@CNF electrode than the latter. Electrochemical impedance spectroscopy (EIS) was also employed to corroborate the claimed stability of the ZnO@CNF electrode. No large changes in impedance parameters were detected in the first 100 cycles at 3 mA cm⁻², suggesting marginal degradation of electrode or electrolyte consumption upon cycles (Figure S20, Table S2). Furthermore, while the measurements reported here were tested with a glyme-based electrolyte, a steep improvement in electrochemical performance was detected even with a commercial carbonate electrolyte, as reported in Note S3 and Figure S21.

Plating Behavior of ZnO@CNF Electrodes. Ex-situ microscopy was used to investigate how the different nucleation behavior would influence the final plating homogeneity. Figure 5 presents the SEM images taken at different magnifications of a flat Cu collector, pCNF and ZnO@CNF electrodes after plating of the same amount of Na at different current densities. In the following is the summary of the observations made from the

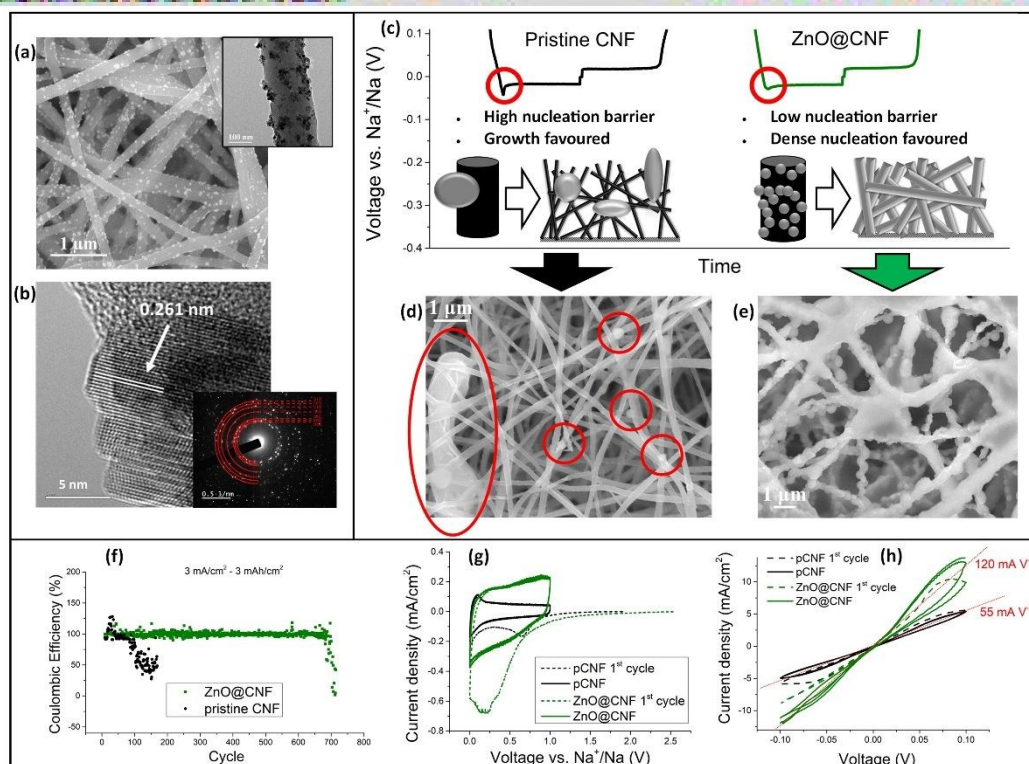


Figure 4: (a) SEM and TEM (inset) images of ZnO@CNF; (b) HRTEM image and SAED (inset) of a ZnO nanoparticle embedded in ZnO@CNF. D-spacing and reflection planes are highlighted. (c) Typical voltage profiles of a plating/stripping cycle for the pristine CNF and ZnO@CNF cells, highlighting the difference in overpotential and illustrating its implications; (d) and (e) SEM images of pCNFs and ZnO@CNFs, respectively, after discharge to 0 V versus metallic Na. (f) Coulombic efficiencies of the pCNF and ZnO@CNF half cells with a loading of 3 mAh cm⁻², measured at a current density of 3 mA cm⁻²; (g) Cyclic voltammetry of half cells made from pCNFs and ZnO@CNFs at a scan rate of 0.1 mV s⁻¹ where the first cycle is represented by a dashed line; (h) Cyclic voltammetry of symmetric cells made from pCNFs and ZnO@CNFs at a scan rate of 0.1 mV s⁻¹ where the first cycle for both materials is represented by a dashed line, while the second and third cycles by solid lines, and the red lines signify the linear fits and the corresponding slopes.

SEM images, comparing the Na deposition behavior of the three different current collectors.

(1) The flat Cu foil current collector possessed a small SSA and low affinity to Na, resulting in a high local current density and a high resistance to nucleation. Figures 5a and 5b show that Na tended to deposit vertically to accumulate into mountain-like structures regardless of the current density, signifying that Na grew preferentially on the previously deposited sites instead of nucleating at new sites. The final micro-morphology exhibited needle-shaped structures of Na dendrites at both currents.

(2) pCNFs had a large SSA due to their 3D network, but low affinity to Na. Thus, the local current density was low, but nucleation was not favored along the fiber length. Na was efficiently incorporated into the scaffold at a low current density, as shown in Figure 5c. Moderately sparse Na nuclei were seen, indicating that the nucleation density was high enough to ensure the containment of Na growth at a low current density because of the large surface area. However, at a higher current density, Na grew uncontrollably to form large agglomerates - so-called "islands" - on the fiber film surface, as shown in Figure 5d and S22. These protuberant structures developed vertically from the film, similarly to the mountain-like structures observed on the Cu foil. Microscopically, a small amount of plated Na was revealed in the fiber network and most of Na was present in the form of "islands". The intense Na signal over F signal in the energy dispersive X-Ray spectroscopy (EDS) elemental map of these agglomerates (Figure S23) indicates that the "islands" could be formed by dry electrolyte salt, confirming they were indeed deposited Na. The EDS map of the area where no "island" was seen highlighted the

presence of additional Na agglomerated below the electrode surface, as seen in Figure S24.

DOI: 10.1039/D0TA05298A

(3) ZnO@CNF had a large SSA and a large number of high-affinity ZnO particles on the fiber surface. As such, the local current density was low, and the nucleation of Na on the whole fiber surface was favored. Figures 5e and 5f confirm that the Na growth took place within the fiber network at both low and high current densities, and no macroscopic agglomeration was observed. The inset images present a quite uniform increase in fiber diameter from 100-150 to 250-300 nm after plating, proving a uniform Na layer was plated on the whole fiber network at both low and high current densities. The EDS elemental maps (Figure S24) support the above finding with little agglomeration compared to pCNF.

Moreover, a thorough study of *ex-situ* SEM images revealed that the gradual increase in fiber diameter caused by Na plating was reproducible and varied depending on the capacity of plated Na, as shown in Figure S25. This observation was unique to ZnO@CNF and was not observed with pCNFs where Na grew in the form of agglomerates. To establish the correlation between the increase in fiber diameter and the applied charge, we formulated a model based on a simple electrochemical principle and geometric consideration. According to the details described in Note S4, the diameter of ZnO@CNF after Na plating can be written as a function of the plated capacity and is given by Equation 3:

$$D_{\text{prediction}} = \sqrt{\frac{4Q}{\pi \cdot L \cdot F} \cdot \frac{M_{\text{Na}}}{\rho_{\text{Na}}} + d_0^2} + t_{\text{SEI}} \quad (3)$$

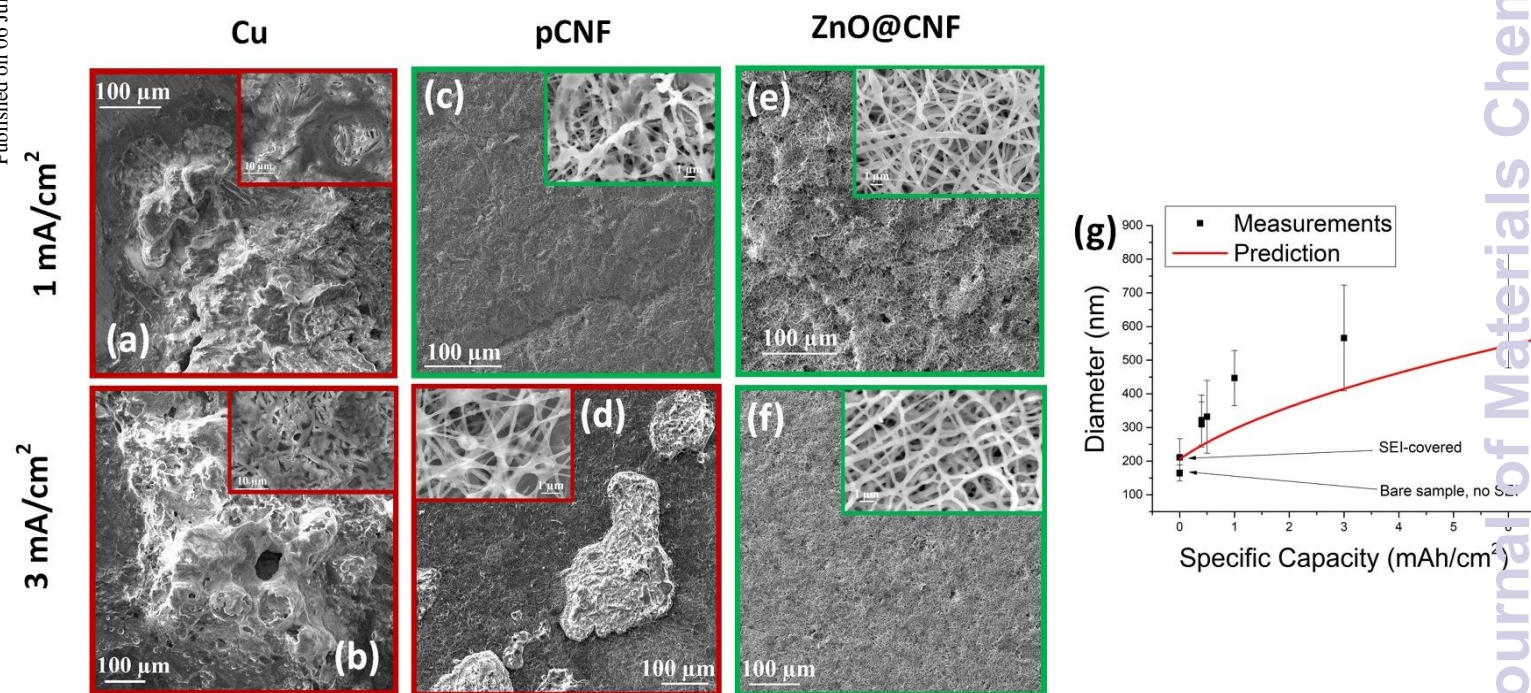


Figure 5: SEM images of Na plated on a Cu current collector (a and b), pCNFs (c and d) and ZnO@CNFs (e and f) taken at low and high magnifications (insets). The current densities used are 1 mA cm⁻² for (a, c and e), and 3 mA/cm² for (b, d and f). The Na loading is 0.4 mAh cm⁻² in all cases. (g) Comparison of fiber diameter between the experimental measurements using *ex-situ* SEM images and the prediction from Equation 3.

where Q is the charge (in Coulomb) applied during plating; L is the total length of fiber network; F is the Faraday constant; M_{Na} is the molar mass of Na and ρ_{Na} is its density; d_o is the diameter of the bare ZnO@CNF fibers; and t_{SEI} is the correction factor representing the increase in diameter after complete Na stripping, which is attributed to the SEI layer. The prediction is compared with the average diameters measured using magnified *ex-situ* SEM images following Na plating under different charging conditions (Figure S25). Moderate accordance between the two was revealed, as shown in Figure 5g, further suggesting a high degree of uniform Na plating on ZnO@CNF. Interestingly, the measured diameters were found independent of applied current density, namely 1 or 3 mA cm⁻², when the applied charge was identical, see Figures S25-2 vs S25-3.

Long-term Cyclic Stability of Symmetric Cells. One of the most promising applications of metal anodes is to be combined with a sulfur or air cathode with a high energy density.^[6, 20] It is thus important to find an efficient way of infusing the alkali metal inside the anode scaffold. To introduce Na in the network, the anode was pre-assembled by stacking the CNF film on top of a pure Na foil. The Na foil was manually pressed into a thickness ranging between 200 and 400 μ m. The use of this stacked design saved materials and processing time better than the classical sacrificial-cell electrodeposition method. The thickness of Na foil could be further reduced using industrial pressing tools. Figure 6a presents a schematic of the stacking scheme of the assembled electrode which allowed Na to be effectively stripped and plated by removal and re-infiltration into the fiber network. Figure 6b presents a side view of the CNF film stacked

on top of a Na layer after 6 mAh cm⁻² of Na were stripped and re-deposited at a current density of 1 mA cm⁻². The image signifies successful re-infiltration of Na in the fiber network after the two-step process. The fiber diameter increased to ~600-800 nm from the initial ~150 nm, proving a large load of deposited Na. The final fiber thickness obtained with the stacked design was compatible with the thickness obtained with regular electrodeposition, indicating that a majority of Na was infiltrated from the initial film into the network. In view of the large variation in the measured Na thicknesses, however, it may be possible that some part of Na had been redeposited back onto the original Na film, as shown in the schematics. The above fiber network was likely to hinder any dendritic growth resulting from this scenario. The overall ZnO@CNF film thickness remained at ~100 μ m after infiltration, suggesting that the network could withstand the mechanical pressure inside of the cell while retaining its original shape. The smooth top view of the same anode shown in Figure S26 indicates that the ZnO@CNF film was able to hold and control the deposited Na even with a high areal loading of 6 mAh cm⁻².

Symmetric CNF-CNF cells (Figure S1c) were assembled by stacking the Na-ZnO@CNF anodes using the aforementioned infusion method. Symmetric Na-Na cells (Figure S1b) were also assembled for comparison. The voltage profiles of symmetric cells prepared at different current densities of 1 and 3 mA cm⁻² with a fixed Na areal loading of 1 mAh cm⁻² are shown in Figures 6c and 6d, respectively. The pure Na cells survived about 200 hr of stable plating/stripping cycles before showing the first short circuit at 1 mA cm⁻² and even poorer performance at a higher current density. In contrast, the ZnO@CNF symmetric cells

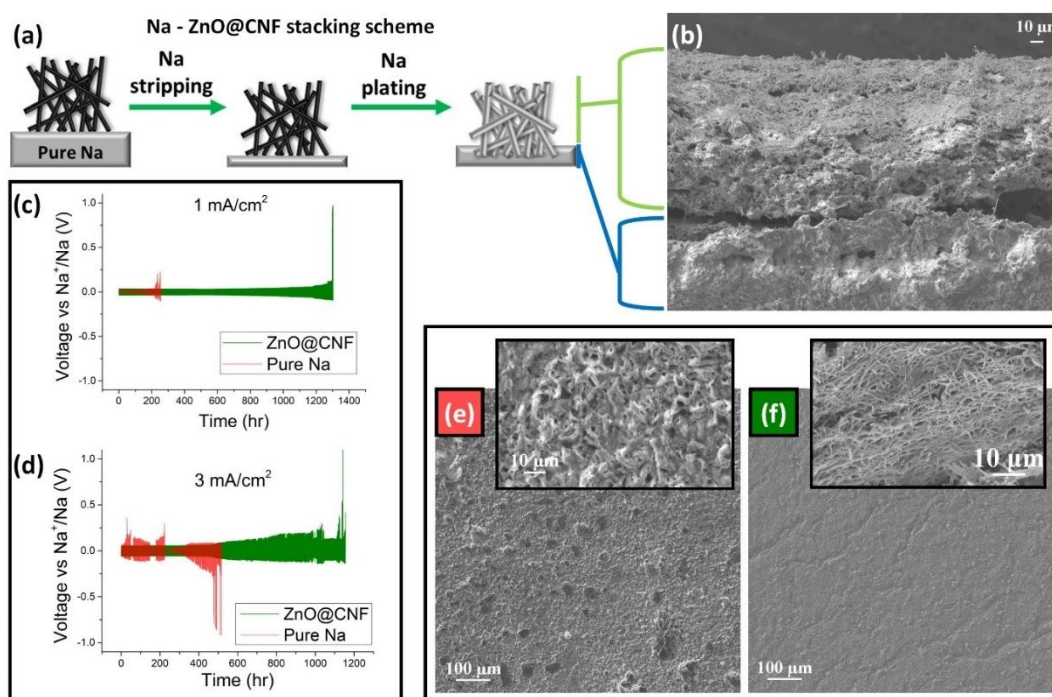


Figure 6: (a) Schematics of the stacking of a pure Na film and ZnO@CNF by network infusion when assembling symmetric cells. (b) Side view of the electrode after stripping followed by plating, highlighting the pure Na residual film (blue) and the layer of Na-infused fibers (green). (c) and (d) Cyclic performance of neat Na and ZnO@CNF symmetric cells measured at 1 and 3 mA cm⁻², respectively. The Na loading is 1 mAh cm⁻² for both cases. (e) and (f) SEM images of the neat Na and ZnO@CNF symmetric cells after 40 cycles at 1 mA cm⁻², respectively.

were able to endure more than 1000 hr of cycles at both current densities without major voltage spikes. The importance of current density as a major factor influencing dendrite formation and cell failure was also highlighted by these findings. The neat Na cells in a symmetric configuration were found to endure a surprisingly long cycle life of 1000 hr at a reduced current density of 0.5 mA cm^{-2} , see Figure S27, but they failed immediately after several cycles at a higher current density of 3 mA cm^{-2} .

Ex-situ microscopy was used to link the electrochemical performance to the electrode plating behavior, as shown in Figure 6e and 6f. Both cells were subjected to 40 cycles at 1 mA cm^{-2} before taking the SEM images. The neat Na electrode presents a very rough and porous surface. The characteristic needle-like dendritic structures with a thick layer ($\sim 100 \mu\text{m}$) of highly porous re-deposited Na was noticed upon closer examination, see Figure 6e. Figure 6f presents the surface morphology of the ZnO@CNF cell showing a smooth surface free from any trace of dendrites, proving that the deposited Na was efficiently contained within the fiber network. The ZnO@CNF electrode retained the initial thickness of $\sim 100 \mu\text{m}$ after 40 cycles (Figure S28), suggesting that the mechanical properties of the structure remained stable even after repeated plating/stripping cycles.

Conclusions

The network of CNFs was explored as a scaffold for stable plating and stripping of Na for Na metal batteries in this work. The following can be highlighted from the experimental studies combined with theoretical calculations:

- (1) A CNF network with a large SSA was fabricated, and its use as a 3D current collector for the plating of metallic Na was studied. The large SSA was found to achieve much improved cyclic stability for a maximum of 1600 cycles at 1 mA cm^{-2} when compared to a flat carbon current collector.
- (2) The affinity between Na and different substrates was analyzed by measuring overpotentials, CEs, and by DFT calculations. The results from these methods suggest that several metals, including Zn and ZnO, could offer a better plating surface than pure carbon. The reaction of Na with a ZnO foil was studied and related to previous *in-situ* studies.
- (3) ZnO@CNF networks with embedded ZnO nanoparticles were fabricated with the addition of a zinc precursor before the electrospinning of fibers. The electrochemical measurements of overpotentials, cyclic voltammetry and SEM images during the first nucleation confirmed that the ZnO nanoparticles integrated in the CNF network acted as preferential plating sites. Consequentially, the ZnO@CNF electrode achieved a much longer cycle life than the pCNF counterpart.
- (4) *Ex-situ* microscopy was used to relate the improved nucleation behavior to the final plating homogeneity: while Na was plated with a poor morphology on a flat Cu current collector at both 1 and 3 mA cm^{-2} , pCNF and ZnO@CNF could distribute the Na loading on a large active surface area. Whereas Na agglomeration was found on the pCNF network,

the improved nucleation behavior of ZnO@CNF resulted in uniform plating at both the low and high current densities.

(5) The thickness of Na layer plated on CNFs under these uniform deposition conditions was predicted based on simple electrochemical principle and geometric considerations, which reasonably agreed with experimental measurements using *ex-situ* SEM images. This work appears to be the first attempt to estimate plating thickness on a porous nanofiber scaffold of metal batteries. The simple model formulated in this study is universal and can be applied to predict plating thickness in different metal batteries having other electrode structures like flat and particle shapes.

(6) Symmetric cells were fabricated using the Na-infused ZnO@CNF electrodes to study the long-term cyclic stability. Cells with ZnO@CNF electrodes survived more than 1000 hr of plating/stripping cycles at both 1 and 3 mA cm^{-2} , whereas pure Na cells suffered short circuits much earlier in less than 200 hr.

Conflicts of interest

There are no conflicts to declare.

Acknowledgements

This project was financially supported by the Innovation and Technology Commission (ITS/001/17) and the Research Grants Council (GRF Projects 16208718) of Hong Kong SAR. A.S. was a recipient of the Hong Kong PhD Fellowship. The authors also appreciate the technical assistance from the Materials Characterization and Preparation Facilities (MCPF) and the Advanced Engineering Materials Facilities (AEMF) of HKUST.

Notes and references

- 1 C. A. Vincent, *Solid State Ionics*, 2000, **134**, 159.
- 2 B. Scrosati, *J Solid State Electrochem*, 2011, **15**, 1623.
- 3 Z. Wen, Y. Hu, X. Wu, J. Han, Z. Gu, *Adv. Funct. Mater.*, 2013, **23**, 1005.
- 4 M. Armand, J. M. Tarascon, *Nature*, 2008, **451**, 652.
- 5 J. B. Goodenough, K. Park, *J. Am. Chem. Soc.*, 2013, **135**, 1167.
- 6 D. Lin, Y. Liu, Y. Cui, *Nat. Nanotechnol.*, 2017, **12**, 194.
- 7 L. Ma, J. Cui, S. Yao, X. Liu, Y. Luo, X. Shen, J. K. Kim, *Energy Storage Mater.*, 2020, **27**, 522.
- 8 B. Lee, E. Paek, D. Mitlin, S. W. Lee, *Chem. Rev.*, 2019, **119**, 5416.
- 9 C. T. Love, O. A. Baturina, K. E. Swider-Lyons, *ECS Electrochem. Lett.*, 2014, **4**, A24.
- 10 Y. Ren, Y. Shen, Y. Lin, C. W. Nan, *Electrochem. Commun.*, 2015, **57**, 27.
- 11 J. Steiger, G. Richter, M. Wenk, D. Kramer, R. Mönig, *Electrochem. Commun.*, 2015, **50**, 11.
- 12 X. Zheng, C. Bommier, W. Luo, L. Jiang, Y. Hao, Y. Huang, *Energy Storage Mater.*, 2019, **16**, 6.
- 13 L. Fan, X. Li, *Nano Energy*, 2018, **53**, 630.
- 14 Y. Zhao, K. R. Adair, X. Sun, *Energy Environ. Sci.*, 2018, **11**, 2673.
- 15 R. Cao, K. Mishra, X. Li, J. Qian, M. H. Engelhard, M. E. Bowden, K. S. Han, K. T. Mueller, W. A. Henderson, J. G. Zhang, *Nano Energy*, 2016, **30**, 825.
- 16 J. Zheng, S. Chen, W. Zhao, J. Song, M. H. Engelhard, J. Zhang, *ACS Energy Letters* (2018), **3**, 315-321.

- 17 Y. Yui, M. Hayashi, J. Nakamura, *Sci. Rep.*, 2016, **6**, 22406.
- 18 W. Luo, C. F. Lin, O. Zhao, M. Noked, Y. Zhang, G. W. Rubloff, L. Hu, *Adv. Energy Mater.*, 2017, **7**, 1601526.
- 19 P. M. Bayley, N. M. Trease, C. P. Grey, *J. Am. Chem. Soc.*, 2016, **138**, 1955.
- 20 W. Xu, J. Wang, F. Ding, X. Chen, E. Nasybulin, Y. Zhang, J. Zhang, *Energy Environ. Sci.*, 2014, **7**, 513.
- 21 X. B. Cheng, R. Zhang, C. Z. Zhao, Q. Zhang, *Chem. Rev.*, 2017, **117**, 10403.
- 22 J. Cui, S. Yao, M. Ihsan-Ul-Haq, J. Wu, J. K. Kim, *Adv. Energy Mater.*, 2019, **9**, 1802777.
- 23 Y. Feng, C. Zhang, B. Li, S. Xiong, J. Song, *J. Mater. Chem. A*, 2019, **7**, 6090.
- 24 G. Huang, J. Han, F. Zhang, Z. Wang, H. Kashani, K. Watanabe, M. Chen, *Adv. Mater.*, 2019, **31**, 1805334.
- 25 Y. Zhou, K. Zhao, Y. Han, Z. Sun, H. Zhang, L. Xu, Y. Ma, Y. Chen, *J. Mater. Chem. A*, 2019, **7**, 5712.
- 26 Q. Dong, B. Hong, S. Hong, H. Fan, C. Gao, Y. Lai, *Electrochim. Acta*, 2018, **284**, 376.
- 27 K. Yan, Z. Lu, H. Lee, F. Xiong, P. Hsu, Y. Li, J. Zhao, S. Chu, Y. Cui, *Nat. Energy*, 2016, **1**, 16010.
- 28 A. P. Cohn, N. Muralidharan, R. Carter, K. Share, C. L. Pint, *Nano Lett.*, 2017, **17**, 1296.
- 29 S. Tang, Z. Qiu, X. Y. Wang, W. W. Wang, Y. Gu, X. G. Zhang, J. W. Yan, M. S. Zheng, Q. F. Dong, B. W. Mao, *Nano Energy*, 2018, **48**, 101.
- 30 S. Tang, Y. Y. Zhang, X. G. Zhang, J. T. Li, X. Y. Wang, J. W. Yan, D. Y. Wu, M. S. Zheng, Q. F. Dong, B. W. Mao, *Adv. Mater.*, 2019, **31**, 1807495.
- 31 M. E. Lee, H. W. Kwak, J. H. Kwak, H. J. Jin, Y. S. Yun, *ACS Appl. Mater. Interfaces*, 2019, **11**, 12401.
- 32 S. Chi, X. Qi, Y. Hu, L. Fan, *Adv. Energy Mater.*, 2018, **8**, 1702764.
- 33 H. Ye, C. Y. Wang, P. F. Wang, P. Wang, T. T. Zuo, Y. X. Yin, Z. J. Zheng, J. Cheng, F. F. Cao, Y. G. Guo, *Nano Energy*, 2018, **48**, 369.
- 34 T. S. Wang, Y. Liu, Y. X. Lu, Y. S. Hu, L. Z. Fan, *Energy Storage Mater.*, 2018, **15**, 274.
- 35 S. Liu, S. Tang, X. Zhang, A. Wang, Q. H. Yang, J. Luo, *Nano Lett.*, 2017, **17**, 5862.
- 36 B. Sun, P. Li, J. Zhang, D. Wang, P. Munroe, C. Wang, P. H. L. Notten, G. Wang, *Adv. Mater.*, 2018, **30**, 1801334.
- 37 H. J. Yoon, N. R. Kim, H. J. Jin, Y. S. Yun, *Adv. Energy Mater.*, 2018, **8**, 1701261.
- 38 Z. Zheng, X. Zeng, H. Ye, F. Cao, Z. Wang, *ACS Appl. Mater. Interfaces*, 2018, **10**, 30417.
- 39 N. Mubarak, M. Ihsan-Ul-Haq, H. Huang, J. Cui, S. Yao, A. Susca, J. Wu, M. Y. Wang, X. Zhang, B. Huang, J. K. Kim, *J. Mater. Chem. A*, doi: 10.1039/d0ta00359j
- 40 H. Ye, S. Xin, Y. X. Yin, Y. G. Guo, *Adv. Energy Mater.*, 2017, **7**, 1700530.
- 41 C. Zhang, Z. Huang, W. Lv, Q. Yun, F. Kang, Q. H. Yang, *Carbon*, 2017, **123**, 744.
- 42 A. G. MacDiarmid, W. E. Jones, I. D. Norris, J. Gao, A. T. Johnson, N. J. Pinto, J. Hone, B. Han, F. K. Ko, H. Okuzaki, M. Llaguno, *Synth. Met.*, 2001, **119**, 27.
- 43 B. Zhang, F. Kang, J. M. Tarascon, J. K. Kim, *Prog. Mater. Sci.*, 2016, **76**, 319.
- 44 B. Zhang, Y. Yu, Z. L. Xu, S. Abouali, M. Akbari, Y. B. He, F. Kang, J. K. Kim, *Adv. Energy Mater.*, 2014, **4**, 1301448.
- 45 Q. Li, S. Zhu, Y. Lu, *Adv. Funct. Mater.*, 2017, **27**, 1606422.
- 46 S. Choudhury, L. A. Archer, *Adv. Electron. Mater.*, 2016, **2**, 1500246.
- 47 S. Chi, X. Qi, Y. Hu, L. Fan, *Adv. Energy Mater.*, 2018, **8**, 1702764.
- 48 S. Tang, Z. Qiu, X. Y. Wang, W. W. Wang, Y. Gu, X. G. Zhang, J. W. Yan, M. S. Zheng, Q. F. Dong, B. W. Mao, *Nano Energy*, 2018, **48**, 101.
- 49 A. Pei, G. Zheng, F. Shi, Y. Li, Y. Cui, *Nano Lett.*, 2017, **17**, 1132.
- 50 C. Yang, Y. Yao, S. He, H. Xie, E. Hitz, L. Hu, *Adv. Mater.*, 2017, **29**, 1702714.
- 51 R. Zhang, X. R. Chen, X. Chen, X. B. Cheng, X. Q. Zhang, C. Yan, Q. Zhang, *Angew. Chem., Int. Ed.*, 2017, **56**, 7764.
- 52 T. Yang, T. Qian, Y. Sun, J. Zhong, F. Rosei, C. Yan, *Nano letters*, 2019, **19**, 7827.
- 53 Y. Teng, M. Mo, Y. Li, J. Xue, H. Zhao, *J. Alloys Compd.*, 2018, **744**, 712.
- 54 S. Sinha, P. N. Didwal, D. K. Nandi, J. Y. Cho, S. H. Kim, C. J. Park, J. Heo, *Ceram. Int.*, 2019, **45**, 1084.
- 55 M. Jing, F. Li, M. Chen, F. Long, T. Wu, *Appl. Surf. Sci.*, 2019, **463**, 986.
- 56 F. Xu, Z. Li, L. Wu, Q. Meng, H. L. Xin, J. Sun, L. Sun, B. Ge, Y. Zhu, *Nano Energy*, 2016, **30**, 771.
- 57 H. Asayesh-Ardakani, W. Yao, Y. Yuan, A. Nie, K. Amine, J. Lu, R. Shahbazian-Yassar, *Small Methods*, 2017, **1**, 1700202.
- 58 Y. Yu, L. Gu, C. Wang, A. Dhanabalan, P. Van Aken, J. Maier, *Angew. Chem., Int. Ed.*, 2009, **48**, 6485.
- 59 B. Zhang, Y. Yu, Z. Huang, Y. B. He, D. Jang, W. S. Yoon, Y. W. Mai, F. Kang, J. K. Kim, *Energy Environ. Sci.*, 2012, **5**, 9895.
- 60 F. Zhang, C. Yuan, J. Zhu, J. Wang, X. Zhang, X. W. Lou, *Adv. Funct. Mater.*, 2013, **23**, 3909.
- 61 Z. L. Xu, S. Yao, J. Cui, L. M. Zhou, J. K. Kim, *Energy Storage Mater.*, 2017, **8**, 10.
- 62 W. M. Haynes, *CRC Handbook of Chemistry and Physics*, 92nd ed., CRC Press, 2011.